https://dx.doi.org/10.1016/j.enconman.2022.115657

Performance evolution analysis of a solid oxide cell operated in fuel-cell, electrolysis and cycle modes

Tonghui Cui [a], Zewei Lyu [a], Minfang Han [a, *], Kaihua Sun [b], Yang Liu [b], Meng Ni [c]

* Corresponding author, E-mail address: hanminfang@mail.tsinghua.edu.cn (M. Han).

[a] Fuel Cell and Energy Storage Center, Department of Energy and Power Engineering, State Key Laboratory of Control and Simulation of Power Systems and Generation Equipment, Tsinghua University, Beijing, 100084, P.R. China

[b] Xuzhou Huatsing Jingkun Energy Co, Ltd., Xuzhou, Jiangsu Province, 221005, China

[c] Department of Building and Real Estate, Hong Kong Polytechnic University, Hung Hom, Kowloon, Hong Kong, China

Abstract: Solid oxide cells (SOCs) are especially important in the context of a boom in the intermittent renewable energy. However, the widespread commercialization of SOCs is still constrained by stability. To investigate the performance evolution mechanisms, fuel-cell, electrolysis, and reversible operations of an industrial-size (10 cm × 10 cm) SOC were conducted. The electrochemical impedance spectroscopy (EIS) measured under open-circuit/a small DC bias and operating current was analyzed employing the distribution of relaxation times (DRT) method and equivalent circuit model (ECM) fitting. Under the fuel-cell and electrolysis modes, the resistances corresponding to the electrode processes held different change trends with increasing DC biases. Compared with the fuel-cell mode, the proportion of the resistance related to the gas diffusion and conversion processes of the fuel electrode was higher in the electrolysis mode. Meanwhile, the resistances associated with the charge transfer reaction, gas diffusion and conversion processes of fuel electrode increased faster in the electrolysis mode. Besides, through the evolution of j-V curves and resistances of electrode processes, the whole operation process was divided into the initial stage (first activation and then rapid-degradation) and the stable stage. In the post-mortem analysis, Ni non-percolating, Ni coarsening and change of pore morphology in the fuel electrode were mainly observed. Combined with the detailed EIS analysis and microstructure changes, the dominant performance evolution mechanism in different stages of the overall operation process was proposed.

Keywords: Solid oxide cells, Performance evolution mechanisms, Ni coarsening, Ni non-percolating

1 Introduction

Solid oxide cells (SOCs) are especially important in the context of continuous increase in the intermittent renewable electricity production, which are regarded as energy conversion and storage devices with high efficiency. SOCs can convert surplus renewable electricity to the chemical energy of H_2 and/or CO by electrolysis of H_2O and/or CO_2, then the stored H_2 and/or CO can be used to generate electricity by fuel-cell mode when the electricity is required [1-3]. Therefore, SOCs have attracted attention and witnessed rapid development recently. However, the commercialization of SOCs is now constrained by their stability.

Extensive work has been conducted to seek for the numerous degradation mechanisms of SOCs. For the oxygen electrode: delamination [4], Sr segregation [5,6], interdiffusion at the electrolyte/oxygen electrode interface [7], and Cr poisoning [8]. For the electrolyte: small pores formation along the grain boundaries[6]. For the fuel electrode: Ni coarsening [9,10], Ni non-percolating [9,11,12], Ni migration [8,9,13],

carbon deposition [14,15], ZrO_2 nanoparticles formation [16] and impurity [6,8,17]. Earlier, crack propagation at the oxygen electrode/electrolyte interface occurring during electrolysis operation at high current densities, which was caused by a high internal oxygen pressure, was considered as an extreme degradation mechanism, especially in the LSM ($La_{1-x}Sr_xMnO_3$) – YSZ (8% Y_2O_3 stabilized ZrO_2) oxygen electrode [4,18]. Currently, at more realistic mild current densities and with LSCF ($La_{1-x}Sr_xCo_{1-y}Fe_yO_{3-\delta}$) or LSC ($La_{1-x}Sr_xCoO_{3-\delta}$) oxygen electrodes applied, microstructure changes occurring in the Ni-YSZ fuel electrode have been considered as primary factors affecting stability. In the Ni-YSZ fuel electrode, YSZ skeleton is relatively stable, while Ni particles microstructural changes are dominant. The underlying mechanisms responsible for the Ni transfer are established [9,19,20]: i) Ni may move from areas with a small radius of curvature to areas with a large radius of curvature to minimize the surface energy. ii) Ni could be transported in the gas phase by vaporization/condensation process under $Ni(OH)_x$ (x may be 2 in SOFC mode, while x may be 1 in SOEC mode) volatile species. iii) Ni may move down the gradient in Ni/YSZ contact angle built inside the electrode during fuel-cell or electrolysis operation. The first and third mechanisms involve a mass transfer at short distances, and the second mechanism is a mass transfer at long distances. These mechanisms may occur together and result in the mostly observed Ni particle changes (coarsening, migration and non-percolating)

Ni coarsening is considered to be a crucial degradation mechanism both in fuel-cell [9,21-23]and electrolysis operations [5,9,24], even in open-circuit condition [25]. Ni coarsening is affected by temperature, humidity, gas flow rate, inert gas applied and initial microstructure, but independent of operation modes. Holzer et al. [25] studied the Ni coarsening in dry and humid atmospheres under open-circuit condition, indicating that the growth of Ni particles in the humid atmosphere was much faster than that in the dry atmosphere. Thermal activation and the effect of gas flow rate were also mentioned. Pihlatie et al. [26] observed that the growth rate of Ni particles in gas with He was faster than that with Ar. Nelson et al. [27] defined the Ni coarsening potential to account for the magnitude of the force driving particle growth, illustrating that significant particle-size difference and volume availability had a high propensity for Ni coarsening. Trini et al. [9] investigated the effects of operation modes on the stability as well as the microstructure changes of Ni-YSZ electrodes under the same operation conditions (gas composition and temperature) except the current direction, suggesting that Ni coarsening occurred in both operation modes. Besides, the YSZ skeleton can restrict the Ni particle growth [27].

Compared with Ni coarsening, Ni migration, i.e., redistribution of Ni of the fuel electrode, is more complicated. Actually, Ni migration has been reported in fuel-cell and electrolysis operations, away from or towards the electrolyte/fuel electrode interface. In general, Ni migration is favored in electrolysis mode than that in fuel-cell mode [9,28]. Hauch et al. [29] discovered that a dense layer of Ni particles formed at the electrolyte/fuel electrode interface after electrolysis operation at high current density (2 $A \cdot cm^{-2}$) and high temperature (950 °C). In the electrolysis operation with a typical temperature range of 650-850 °C, the Ni migration away from electrolyte/fuel electrode interface has been mainly reported in the current literatures [5,9,13] and is considered to be one of the dominating degradation mechanisms. In this situation, a higher porosity layer near the interface and a denser layer next to the porous one are usually left. As for fuel-cell mode, Menzler et al. [8] detected Ni migration towards the electrolyte after a 10-years operation, with enriched Ni amount and reduced porosity. Besides, Ni migration away from the electrolyte/fuel electrode interface was also reported under fuel-cell mode [21-23]. Some hypotheses have been proposed to understand the underlying mechanisms of Ni migration [9,20,21]. Ni migration towards the interface under electrolysis operation and away from the interface under fuel-cell operation can be simply ascribed to the $Ni(OH)_x$ species migration down the

steam partial pressure gradients [30]. While the other two cases, i.e., Ni migration away from the interface under electrolysis operation and towards the interface under fuel-cell operation, can be qualitatively explained by some hypotheses. Mogensen et al. [20] considered loss of contact between Ni-YSZ or Ni particles as a prerequisite for Ni migration, and then local potential gradients caused the $Ni(OH)_x$ to migrate down the local redox potential gradients. $Ni(OH)_x$ species may migrate by surface diffusion below 800 °C or in gas phase above 900 °C. Trini et al. [9] presented another hypothesis in which the Ni-YSZ contact angle gradients were believed to be the driving force for Ni migration. An oxygen potential gradient between the reaction area and support layer was established during operation, resulting in the gradient in contact angle. Then, Ni will move from the region of high contact angle (low wettability) to the region of low contact angle (high wettability), i.e., down the chemical potential. Besides, Lyu et al. [21] proposed a fast Ni migration mechanism during short-term operation based on the Ni coarsening potential [27], that is, smaller Ni particles in the active layer were prone to migrate towards the support layer with larger Ni particles.

Moreover, Ni non-percolating is that the Ni particles lose electrical contact with each other, and depletion of percolating Ni near the electrolyte/fuel electrode interface has been reported in many literatures [9-13,17,21,31]. Depletion of percolating Ni and Ni migration are often confused, but the two are different. Similar to Ni migration, depletion of percolating Ni is much more pronounced in electrolysis operation than that in fuel-cell operation [9]. However, unlike Ni migration, depletion of percolating Ni has no direction. Less attention has been paid to the mechanism of Ni non-percolating compared to Ni migration, although both can cause serious damage to the cell performance. Meanwhile, the mechanism of depletion of percolating Ni is still smeared. Some studies presented that the depletion of percolating Ni was much severer at the fuel electrode inlet than that at the outlet under electrolysis operation, and the higher steam partial pressure and overpotential were considered to be the reason for the larger degradation at the inlet [9,11,12].

In summary, the composition, microstructure and operating conditions of SOCs have a great influence on the dominant degradation mechanism. In particular, the degradation mechanism of the Ni-YSZ electrode is still unclear and under intense debate. On the other hand, the performance evolution is extremely complex and has various trends in different operation stages, which indicates that the dominant performance evolution mechanism is different. Many literatures have reported the complex performance changes. Some studies found that the performance declined fast and then recovered, attributing to Si species from the applied glass-sealing [29] and impurities in the gas stream (most likely S) [32], which were harmful to the fuel electrode. Moreover, Koch et al. [33] observed that the performance improved and then dropped slowly. And they concluded that this phenomenon was due to the activation and passivation of the oxygen electrode during the constant current because the impedance between 1 and 200 Hz was strongly affected. In most of the current literatures, rapid degradation firstly and then a stable state can be discovered [17,34,35]. Therefore, the complicated operation stages and related performance evolution mechanisms still need to be explored. In terms of research methods, in most of the studies, the degradation mechanisms were analyzed based on EIS under different DC biases, some were based on EIS under open-circuit condition [36,37] or a small DC bias [38,39], while others were based on EIS under operating current [17,40]. It is not clear whether the evolution of EIS under different DC biases is the same, that is, whether it affects the judgment of the degradation mechanisms.

Therefore, in this study, fuel-cell, electrolysis, and reversible operations of an industrial-size SOC were conducted. To have an in-depth understanding of the performance evolution mechanisms, the EIS

spectra measured under open-circuit, small DC biases and operating current were analyzed in detail. Meanwhile, the performance and stability of fuel-cell and electrolysis modes were analyzed and compared. Moreover, the post-mortem analysis of the fuel electrode was emphasized to investigated the microstructure changes of Ni particles. Through the electrochemical and post-mortem analyses, the dominant performance evolution mechanism in different stages of the overall operation process was proposed. The results will lay a foundation for improving the stability of SOCs.

2 Experimental

The cell used in this work is a fuel electrode supported SOC cell with an effective area of 10 cm × 10 cm, which is supplied by Xuzhou Huatsing Jingkun Energy Co. Ltd. The cell consists of a Ni-YSZ support layer, a Ni-YSZ active fuel electrode layer, a YSZ electrolyte layer, a GDC ($Gd_{0.1}Ce_{0.9}O_{2-\delta}$) interlayer, and a LSCF ($La_{0.6}Sr_{0.4}Co_{0.2}Fe_{0.8}O_{3-\delta}$)-GDC oxygen electrode layer. More details about cell preparation and assembly can be found in Ref [21].

The cell was heated to 720 °C and the reduction of NiO particles in the fuel electrode lasted for about 4 h. Then, the performance was characterized and the cell operated at a constant current density of 0.1 $A \cdot cm^{-2}$ for about 16 h at 720 °C. After that, the performance was tested at various temperatures (720, 800 °C) with 3 slm (standard liter per minute) air supplied to the oxygen electrode and 1 slm H_2 to the Ni-YSZ electrode. Afterward, fuel-cell, electrolysis, and reversible operations were carried out at 800 °C in turn. As for details, the current densities of the three stages were +0.3, -0.3, and -0.3/+0.3 $A \cdot cm^{-2}$, respectively, and all the three stages lasted for about 150 h. The reversible operation was performed with periods of about 7 h and 15 h in electrolysis and fuel-cell modes respectively every day, with the remaining time used for mode switching and electrochemical tests. 1 slm H_2 was supplied to the fuel electrode during fuel-cell mode operation, while 2 slm H_2/H_2O gas mixture (50 vol.% H_2O, 50 vol.% H_2) was provided during electrolysis mode operation. 3 slm air was supplied to the oxygen electrode in the two modes. The cell was periodically characterized by j-V curves and EIS measurements during operation. For the j-V curve measurements, the current was stepwise increased with 1 A per step by electronic load (Kikusui PLZ664WA) and DC power (EA-PSI 8080-60). A dwell time of 12 s was conducted at each current. An electrochemical workstation (Zahner IM6) and a home-designed circuit were employed to measure the EIS spectra under different DC biases. More details about EIS test devices can be found in Ref [21]. The frequency range for EIS measurements was from 100 kHz to 0.2 Hz, with 12 points per decade and an AC of 1 A.

Two cells were characterized for post-mortem analysis, which had the same fuel electrodes. In addition to the above tested cell (named aged cell), a cell exposed to reduction only (named reference cell) was selected to assess microstructure changes of the fuel electrode. Pieces of cross-sections of the cells were vacuum embedded in epoxy resin, followed by being ground and polished. A Zeiss Gemini SEM 500 FE-SEM (Field Emission Gun Scanning Electron Microscope) was employed for obtaining high-resolution micrographs. To distinguish the percolating of Ni particles in the Ni-YSZ fuel electrodes, cross-section samples without platinum coating were characterized using an Inlens detector and an acceleration voltage of 1 kV. The low-voltage SEM method was developed by Thydén et al. [41] and later applied in many studies [9,17,42]. Moreover, to characterize the microstructure and quantify the porosity of the fuel electrode, the cross-section samples with platinum coating were inspected by a BSD detector and an accelerating voltage of 10 kV. The BSD images of the fuel electrodes were analyzed using ImageJ software to evaluate the porosity variation in the direction perpendicular to the electrode/electrolyte interface.

3 Results and discussion

3.1 Overall operation process

The complete time plot of the overall operation process is shown in Fig. 1, with roman numerals marking the distinct operation periods. Detailed test conditions can be found in the Experimental Section. Period I, II, IV, VI were initial, fuel-cell, electrolysis, and reversible operation, respectively. It should be noted that the voltage degradation from 32 h to 48 h was significantly faster than that from 53 h to 192 h, although both operated at +0.3 $A \cdot cm^{-2}$ at 800 °C. Therefore, the first 50 h, which may be accompanied by rapid microstructure changes, was considered as the initial stage and studied separately. In the subsequently more stable state, the degradation mechanisms of the fuel-cell and electrolysis operations were discussed emphatically. Period III and V were accidents during the experiment due to misoperation and a failure in the steam supply system, which were not focused on in this paper.

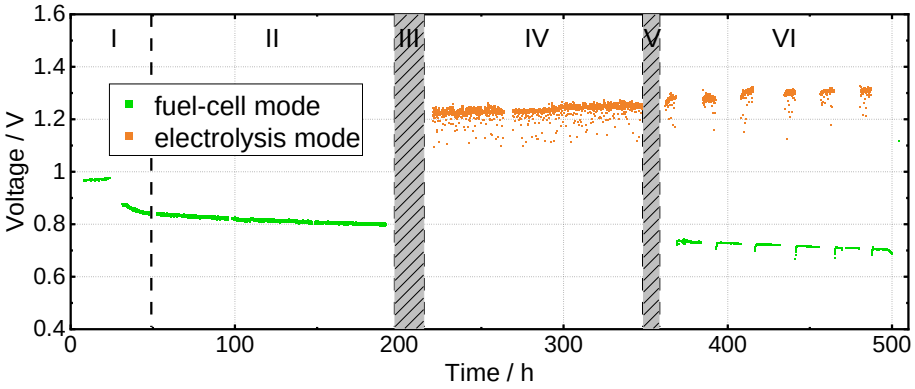

Fig. 1. Time plot of the overall operation process.

3.2 Initial performance evolution

Fig. 2(a) shows the j-V curves in the initial stage. The j-V curves measured at 5 h and 24 h basically coincided with each other, and the power density was 0.33 $W \cdot cm^{-2}$ under a voltage output of 0.7 V at 720 °C, indicating that the performance was unchanged. However, the performance deteriorated rapidly from 30 h to 48 h and the power density decreased from 0.483 $W \cdot cm^{-2}$ to 0.398 $W \cdot cm^{-2}$ under a voltage output of 0.7 V at 800 °C. The performance evolution was consistent with the output voltage variation shown in Fig. 1.

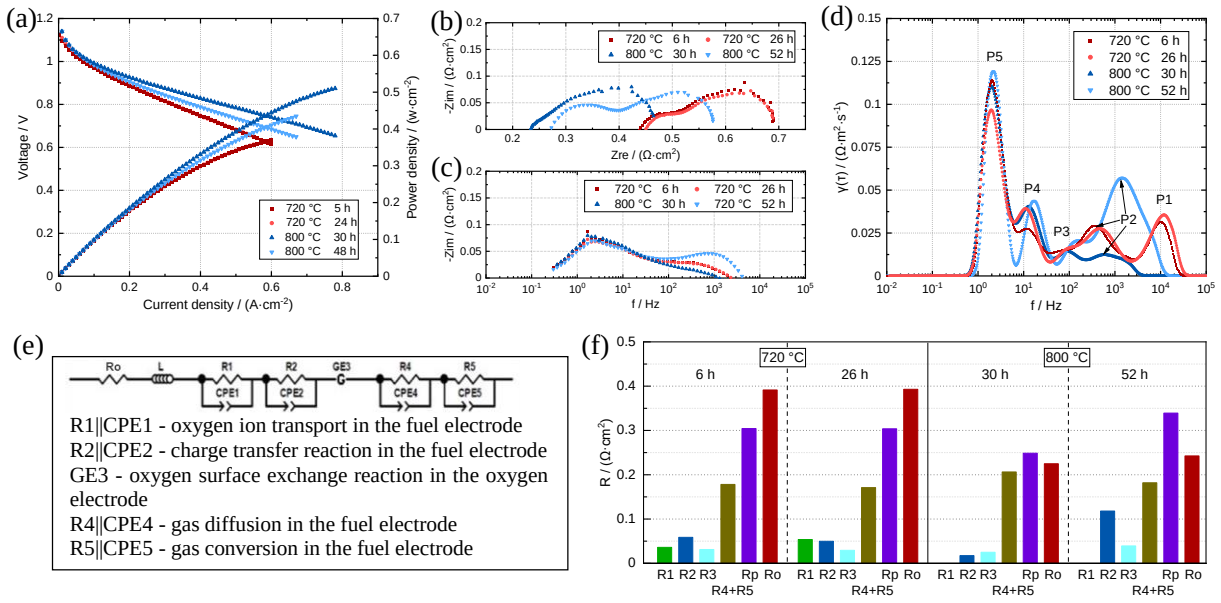

Fig. 2. j-V curves (a), Nyquist plots (b), Bode plots (c), DRT results (d) and ECM results (f) in the initial stage. And the applied ECM model and the corresponding electrode processes of each element (e). The EIS, DRT and ECM results were under +0.3 A·cm^{-2}. 1 slm H_2 and 3 slm air were supplied to the fuel electrode and the oxygen electrode, respectively.

To understand the reasons for the performance evolution, the EIS measurements were conducted in the initial stage, as demonstrated in Fig. 2(b) and (c). During 6 h-26 h (named activation stage), a slight shrinkage of the low-frequency arc can be observed, while the most significant phenomenon during 30 h-52 h (named rapid-degradation stage) was the sharp increase of high-frequency arc. The ohmic resistance can be roughly represented by the intersection of the high-frequency spectra with the real-axis and increased in both stages. And the ohmic resistance in the rapid-degradation stage increased faster, which may be caused by two factors: the higher the temperature, the faster the ohmic resistance of metallic interconnector increased [43]; the changes of electrode microstructure led to longer ions/electrons transport path, such as Ni redistribution and non-percolating [38].

Then, the distribution of relaxation times (DRT) method analysis was performed to identify the highly overlapping physical/chemical processes involved in EIS and qualitatively estimate the contributions of different processes, as shown in Fig. 2(d). Five characteristic peaks (from high frequency to low frequency, the sequence is P1-P5) can be distinguished from the DRT plots, associating with distinct physical/chemical processes. The resistance of each process can be represented by the integral area covered by the corresponding characteristic peak. In our previous studies, the corresponding relationship between characteristic peaks and physical/chemical processes on the same type of cells was systematically analyzed, including button cell and 10 cm ×10 cm industrial-size cell [44,45]. Combined with those in the literatures [46-49], the correspondence can be summarized as follows: P1 is considered to be the oxygen ion transport in the composite electrodes. The oxygen electrode used in this paper is the LSCF-GDC oxygen electrode, in which the ionic conductivity of GDC is high, thus P1 mainly comes from the Ni-YSZ fuel electrode. However, P1 is susceptible to inductance in the testing loop [49], especially in the EIS measurements of large-size cells.

P2 is ascribed to the charge transfer reaction at the triple-phase boundaries (TPB) in the fuel electrode. P3 is associated with the oxygen surface exchange reaction in the oxygen electrode. P4 and P5 are primarily related to the gas diffusion and gas conversion processes in the fuel electrode, respectively. Since the oxygen electrode is thin, gas diffusion and gas conversion processes can only be observed at very low oxygen partial pressure (5%) and flow rate [46,48]. And the gas diffusion and gas conversion processes are usually coupled [49]. Moreover, in the middle frequency range, the oxygen surface exchange reaction tends to overlap with the gas diffusion process [45,46]. Nevertheless, the DRT analysis is still a very important method to parse EIS. Furthermore, to quantitatively split up the contributions of the different electrode processes, the EIS data were fitted with equivalent circuit model (ECM) making use of the complex nonlinear last square (CNLS) method and the fitted resistance values are shown in the Fig. 2(f). Fig. 2(e) presents the applied ECM model, which is composed of four constant phase elements RQ and a Gerischer element (G), and these five elements match the characteristic peaks in DRT results. A Rohm and an inductor (L) are also included. The DRT calculation and ECM fitting were performed using a homemade Python program (named EISART). The EIS fitting results were satisfactory, and the relative errors of the real and imaginary parts were basically within ±2%.

In the DRT results, the most obvious distinction was the evolution of the P2 peak, as presented in Fig. 2(d). P2 was essentially unchanged in the activation stage, while rose significantly in the rapid-degradation stage. Further, Fig. 2(f) showed that R2 increased from 0.017 $\Omega \cdot cm^2$ to 0.118 $\Omega \cdot cm^2$, which was the major cause of performance deterioration during the rapid-degradation stage. Besides, R4&R5 delivered a slight decline in both stages, from 0.178 $\Omega \cdot cm^2$ to 0.171 $\Omega \cdot cm^2$ in the activation stage and from 0.206 $\Omega \cdot cm^2$ to 0.182 $\Omega \cdot cm^2$ in the rapid-degradation stage. The above changes in resistances were related to the rapid change of the fuel electrode microstructure during the initial stage. In our previous studies with the same batch cells, the increase of fuel electrode porosity and then the enrichment of the gas-phase diffusion process were believed to result in the slight increment of performance in the activation stage [50]. Meanwhile, the fast Ni coarsening due to the particle size difference between the active layer and the support layer, as well as the Ni redistribution and non-percolating in the active layer, were considered to be the leading factors for the performance degradation in the rapid-degradation stage [21]. These research results can explain the changes of R2 and R4&R5 in this paper. It is worth noting that although the phenomenon (first activation and then rapid-degradation) in the initial stage was consistent for the same batch cells, the duration and performance variation of the two stages were different [21,50,51]. This may be related to operating conditions, such as temperature, current, and steam partial pressure of the fuel electrode. Another possible factor is the subtle differences in electrode microstructure. More detailed studies are needed to investigate the influence of operating conditions and microstructure on the initial stage.

3.3 Comparison of fuel-cell and electrolysis modes

The j-V curves were periodically measured, as demonstrated in Fig. 3. Fig. 3(a) and Fig. 3(b) exhibit the j-V curves at 800 °C in fuel-cell mode and electrolysis mode, respectively. In fuel-cell operation, the performance deteriorated rapidly from 30 h to 48 h and the power density decreased by 0.085 $W \cdot cm^{-2}$ under a voltage output of 0.7 V. While over the next 144 h, a slower decline took place in the performance and the power density decreased by 0.087 $W \cdot cm^{-2}$ in total. The evolution of the performance indicated that it was reasonable to take the first 50 h as the initial stage for research. As for electrolysis operation, the voltage increased from 1.212 V to 1.256 V during 219 h-312 h. In reversible operation, the performance reduced slowly both in fuel-cell mode and electrolysis mode.

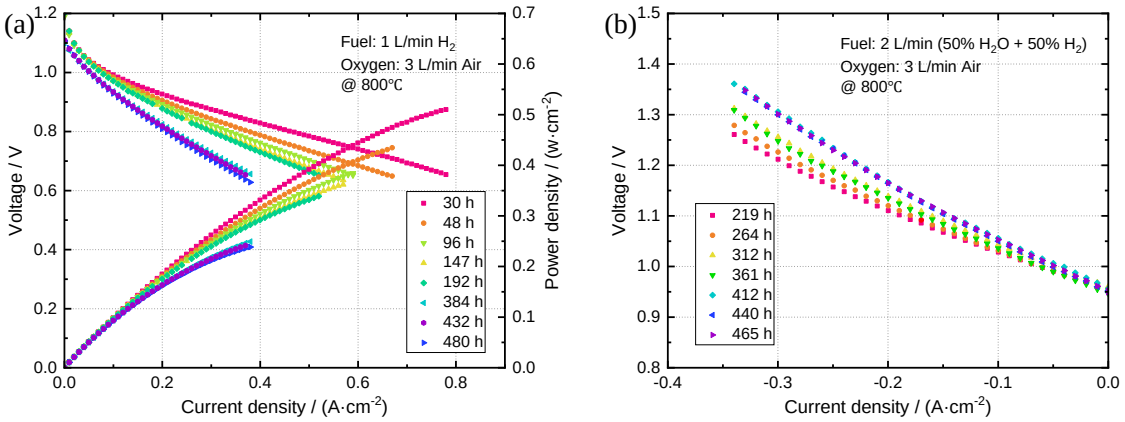

Fig. 3. j-V curves in fuel-cell mode (a) and electrolysis mode (b) at 800 °C

To explore the mechanisms of performance evolution, the EIS measurements under open-circuit/a small DC bias and operating current were carried out in both fuel-cell and electrolysis operations. And the corresponding DRT analysis and ECM fitting were performed, aiming to compare the evolution of different electrode processes under different DC biases. The Nyquist plots, Bode plots, DRT results, applied ECM model, and resistances under different DC biases can be seen in Fig. 4 (fuel-cell operation) and Fig. 5 (electrolysis operation).

Fig. 4 clearly exhibits the influence of DC biases on each resistance in fuel-cell mode. With increasing the DC biases, the polarization resistance (Rp) shrunk significantly and the ohmic resistance (Ro) remained unchanged. The polarization resistance was further decomposed, indicating that R1 (related to oxygen ion transport in the fuel electrode) was independent of the DC biases. While R2 (ascribed to charge transfer reaction in the fuel electrode), R3 (associated with the oxygen surface exchange reaction in the oxygen electrode), and R4&R5 (corresponding to gas diffusion and gas conversion processes) dramatically decreased with increasing the DC biases. Besides, the P2, P3, P4, and P5 peaks shifted towards higher frequency in DRT results. The changes of resistances with DC biases can be explained by theoretical derivation, as presented in the work of Lyu et al. [34]. The conclusion was in agreement with the experimental results in this paper.

Although the values of resistances varied with DC biases, the evolution trend of resistances was basically the same under different DC biases, which indicated that in terms of resistances, the DC biases did not affect the judgment of the degradation mechanisms. Nevertheless, EIS measurements under different DC biases are necessary to quantitatively calculate the output voltage degradation caused by each electrode process. Lyu et al. [21] successfully distributed the overall voltage degradation to each electrode process in fuel-cell mode, the corresponding research in electrolysis mode needs to be carried out further. As presented in Fig. 4(1-d) and (2-d), the results of the initial stage were also included for comparative analysis. Ro, R1, and R3 approximately linear changed during 30 h-194 h. Nevertheless, the evolution of R2, R4&R5, and Rp can obviously be divided into two stages. Different from the rapid-degradation stage (from 30 h to 52 h) mentioned in Section 3.2, R2 was essentially unchanged and R4&R5 showed a slight increase after 50 hours. Combining the evolutions of voltage in Fig. 1 and performance in Fig. 3, it was considered that the cell reached a relatively stable degradation stage after 50 hours.

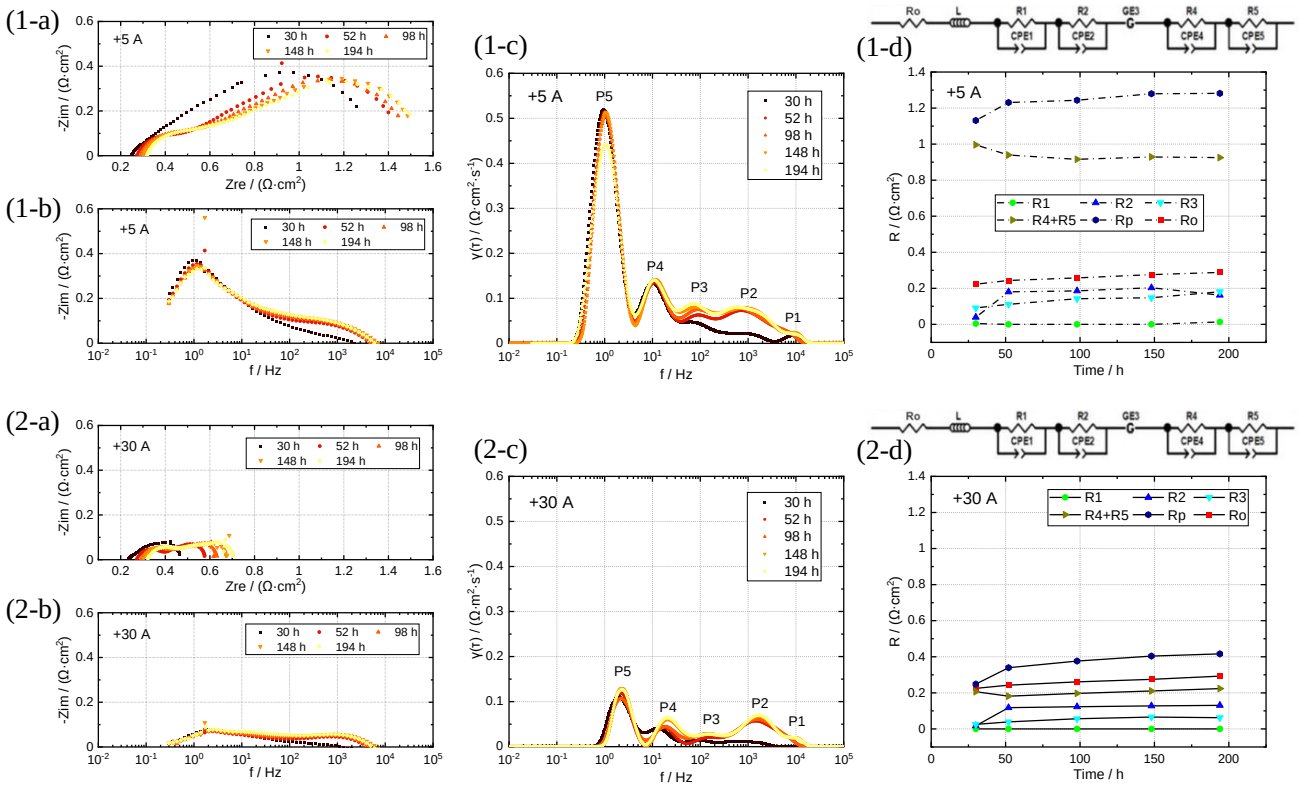

Fig. 4. The Nyquist plots (a), Bode plots (b), DRT results (c), applied ECM model and fitted resistances (d) under +0.05 A·cm^{-2} (1) and +0.3 A·cm^{-2} (2) in fuel-cell operation at 800 °C. Feeding 1 slm H_2 to the fuel electrode and 3 slm air to the oxygen electrode.

The influence of DC biases on each resistance in electrolysis mode is displayed in Fig. 5. The ohmic resistance (Ro) remained unchanged, while contrary to fuel-cell mode, the polarization resistance (Rp) increased significantly with increasing the DC biases. R2, R3, R4, and R5 contributed to the increase of Rp. Moreover, the P2, P3, P4, and P5 peaks shifted towards lower frequency in DRT results with increasing the DC biases. Even under the same steam and hydrogen partial pressure, the trends of resistances of fuel-cell mode and electrolysis mode vary differently with the DC biases. This phenomenon is called the asymmetry behavior between the two modes. Besides, asymmetric behavior is also reflected in the higher overpotential in electrolysis mode under the same current, steam and hydrogen partial pressure. Kishimoto et al. [52] investigated the asymmetric behavior between the two operation modes under the same steam and hydrogen partial pressure. The electrochemical experiments and numerical simulations were conducted, indicating that the asymmetry was originated from unequal charge-transfer coefficients firstly. More importantly, under DC biases, the hydrogen and steam partial pressure inside the electrode were inconsistent, and gas diffusion was different because of Knudsen diffusion. Ebbesen et al. [53] considered that the temperature difference between the two modes caused by electrochemical experiments was one of the factors of asymmetry. The effect of gas diffusion and conversion processes on asymmetry was also mentioned. Hence, gas diffusion and conversion processes in the fuel electrode are much important in the electrolysis mode. Optimizing the microstructure of fuel electrodes, such as porosity [53] and pore size [52], is an effective means to enhance gas diffusion, reduce asymmetry and improve the performance of electrolysis mode.

Similar to fuel-cell mode, the evolution trend of resistances was basically the same under different DC biases in the electrolysis mode, as presented in Fig. 5(1-d) and (2-d). R2, R4&R5, Rp and Ro increased gradually over time, while R3 showed a slight downward trend.

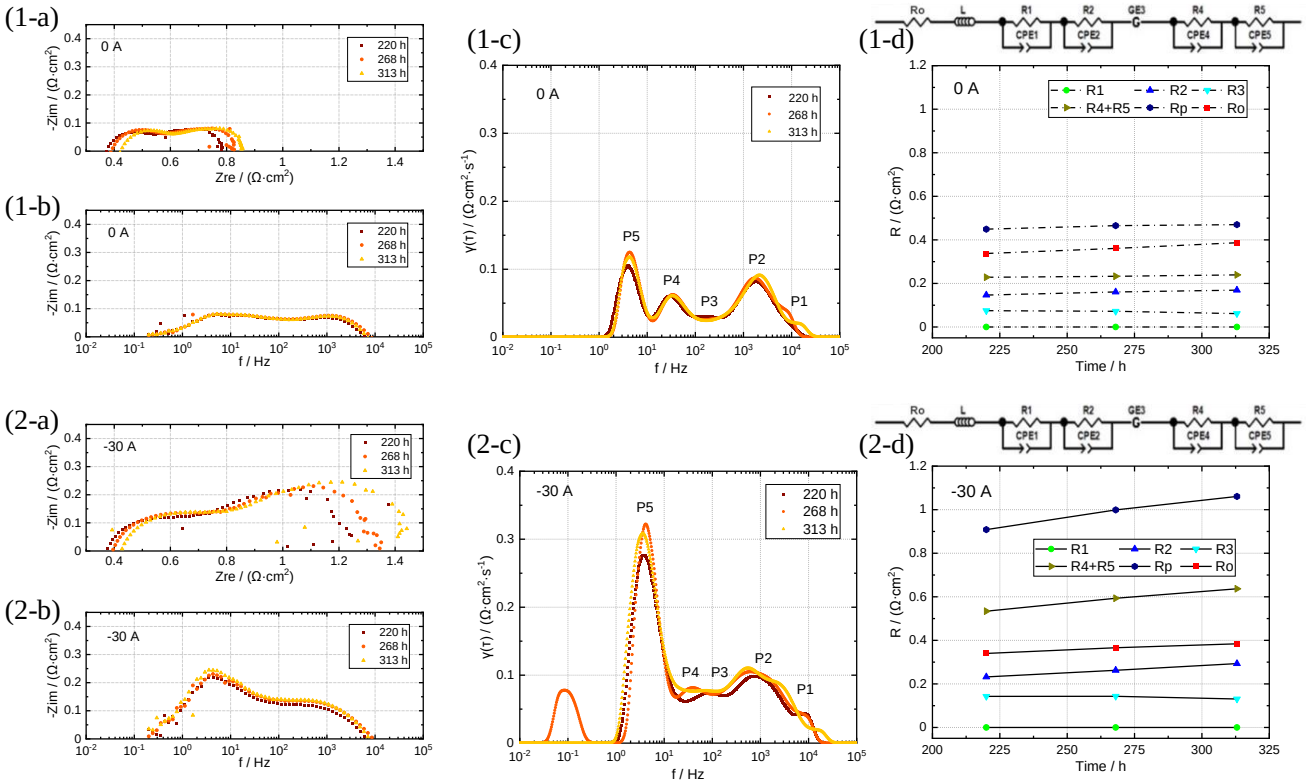

Fig. 5. The Nyquist plots (a), Bode plots (b), DRT results (c), applied ECM model and fitted resistances (d) under open-circuit (1) and +0.3 A·cm^{-2} (2) in electrolysis operation at 800 °C. Feeding 2 slm H_2/H_2O gas mixture (50 vol.% H_2O, 50 vol.% H_2) to the fuel electrode and 3 slm air to the oxygen electrode.

As mentioned above, the cell reached a stable degradation stage after 50 hours, so the difference between the fuel-cell mode and the electrolysis mode can be analyzed using the data after 50 hours. Since the evolution trend of resistances was basically the same under different DC biases in both modes, the evolution of resistances under the operating current (±0.3 A·cm^{-2}) was selected from Fig. 4 and Fig. 5 for comparison, as presented in Fig. 6. Compared with the fuel-cell mode, Rp obviously increased faster in the electrolysis mode as shown in Fig. 6(a). Furthermore, R2 and R4&R5 were the main contributors to the faster growth of Rp. These phenomena are closely associated with the microstructure of the fuel electrode. Trini et al. [9] investigated the impact of operation mode on microstructure changes, with the same fuel inlet gas composition (50 vol.% H_2O, 50 vol.% H_2). The resistance contributed to the Ni-YSZ electrode increased much faster in electrolysis mode than that in fuel-cell mode. And the post-mortem analysis highlighted that Ni migration away from the electrolyte/fuel electrode interface and depletion of percolating Ni were detected only in the electrolysis mode, while Ni coarsening was independent of the operation mode. Therefore, the more serious Ni migration and non-percolating of the fuel electrode may be the reason for the rapid increase of R2 in the electrolysis mode. Although Ni coarsening is independent of operation modes, the high

steam partial pressure of the fuel electrode could promote Ni coarsening [25]. In this paper, the steam pressure of support layer in the electrolysis mode may be higher than that in fuel-cell mode. Therefore, the more serious Ni coarsening may also result in a rapid increase of R2 and R4&R5 in the electrolysis mode. Many studies suggested that Ni migration away from the electrolyte/fuel electrode interface and depletion of percolating Ni would prolong the oxygen ion transport path, leading to an increase in ohmic resistance [10,38,54]. However, the ohmic resistance increased at a similar rate in the two modes in this paper, and the possible reason could be that the metallic interconnects contributed a large part to the ohmic resistance. The R3 was small and easily overlapped with the gas diffusion process when fitting, which may lead to the irregular changes of R3 in Fig. 6. Moreover, we can observe that the proportions of R1, R2 and R3 in the total resistance in the electrolysis mode were basically the same as that in the fuel-cell mode, while the proportion of R4&R5 was higher and the proportion of Ro was lower in the electrolysis mode. Once again, promoting gas diffusion and conversion process is an important way to improve the performance of electrolysis mode.

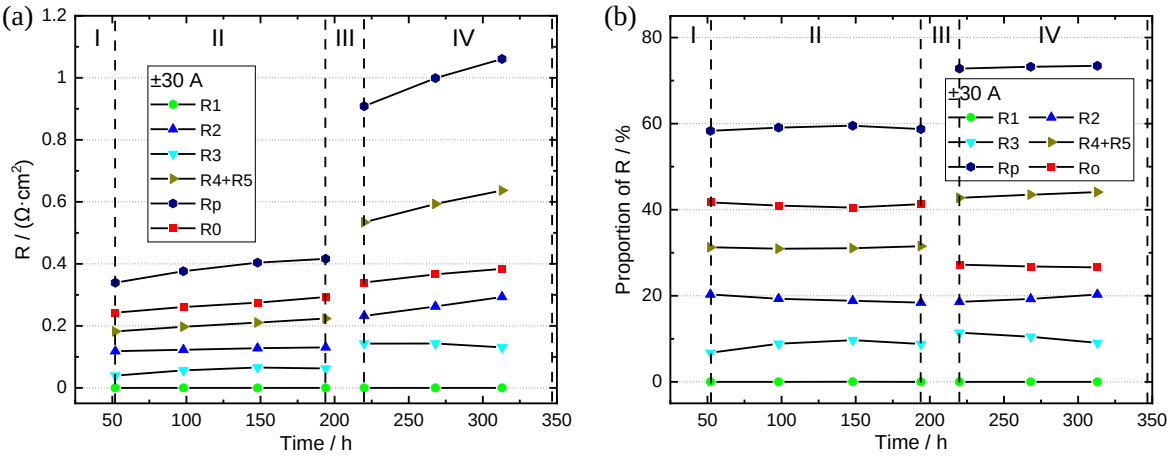

Fig. 6. Resistances (a) and proportions of each resistance in the total resistance (b) over time.

A brief summary of the electrochemical analysis is given. Through the evolution of j-V curves and resistances of electrode processes, the whole operation process was divided into the initial stage (about 0-50 h) and the stable stage. The cell performance first showed slight change (activation stage) and rapidly declined subsequently (rapid-degradation stage) in the initial stage, while decreasing slowly and linearly in the stable stage. Gas diffusion and conversion processes were considered to be the primary factors of the performance variation in the activation stage, and the charge transfer reaction of the fuel electrode dominated the rapid-degradation stage. Moreover, in the stable stage, the comparison of the fuel-cell operation and electrolysis operation was conducted, indicating that the resistances associated with charge transfer reaction, gas diffusion and conversion processes of fuel electrode increased faster in the electrolysis mode. And the importance of the gas diffusion process to the electrolysis mode was emphasized. Therefore, the electrode processes associated with the fuel electrode were significant for the performance and stability of SOCs. Furthermore, the post-mortem analysis should be performed to determine the microstructure changes of the fuel electrode.

3.4 Discussion on the microstructure changes in Ni-YSZ electrode

Fig. 7 presents the low-voltage SEM and BSD images of the polished cross-sections of the fuel

electrodes, containing a cell only reduced (reference cell) and the cell in this paper (aged cell). Compared to the reference cell, the depletion of percolating Ni particles near the electrolyte/fuel electrode interface was clearly observed in the aged cell, as shown in Fig. 7(a) and (d). And the width of the depletion region of percolating Ni reached about 6 μm. Moreover, in the fuel electrode support layer in the aged cell, non-percolating Ni particles were also found, while the Ni particles in the reference cell were percolated throughout the fuel electrode. A contrast under higher magnification was more clearly in Fig. 7(b) and (e), where the red arrows pointed out the non-percolating Ni particles in the support layer. Besides, in the aged cell, we discovered that the size of Ni particles increased and the shape seemed to change from elongated and irregular to round. Ni coarsening, accompanied by shape changes, may lead to depletion of percolating Ni. In this paper, depletion of percolating Ni was found in both the active and support layers, which provided evidence for this explanation. However, depletion of percolating Ni of the active layer is usually more serious than that of the support layer, as shown in this paper and other studies [9,12,17]. This may be because that the wettability of Ni on YSZ is weakening with the increase of polarization under electrolysis operation according to Jiao et al. [55]. Under fuel-cell operation, the high steam partial pressure in the reaction area will increase the Ni particle growth rate [25], which results in deterioration of contact between Ni particles. Ni non-percolating was much severer at the fuel electrode inlet than that at the outlet under electrolysis operation [9,11,12], which is another example of the effect of polarization and steam partial pressure.

Fig. 7(c) and (f) presents the dramatic changes in the fuel electrode pores. The pores in the reference cell were elongated and appeared to be connected, while the pores in the aged cell were round and less connected. Furthermore, the porosity at the active/support layer interface appeared to improve in the aged cell through comparing Fig. 7(b-c) and (e-f). And the high porosity layer had a certain relationship with the depletion region of percolating Ni, as shown by the yellow dotted lines. Therefore, twenty SEM images of each cell were analyzed to obtain the average porosity of the fuel electrode. Eight regions were taken from each image and the average porosity of each region was estimated. The regions were with a width of about 2 μm and a length of about 56 μm, as shown in the red rectangles in Fig. 8(a). And the quantitative results of porosity were presented in Fig. 8(b). In the reference cell, the porosities were about 27% in the region 0-4 μm, 23% in the region 4-6 μm, and 19% in the region 6-16 μm away from the electrolyte/fuel electrode interface. In the aged cell, the porosities were similar to the reference cell in the region 0-4 μm and 8-16 μm, being about 28% and 21%. The slightly higher porosity of the aged cell could be due to Ni coarsening or subtle differences in the initial microstructure. Nevertheless, the porosity in the region 4-8 μm was significantly higher than that in the reference cell, which was about 30%. This suggested that Ni migration may have occurred in the region, which is usually accompanied by a change in porosity.

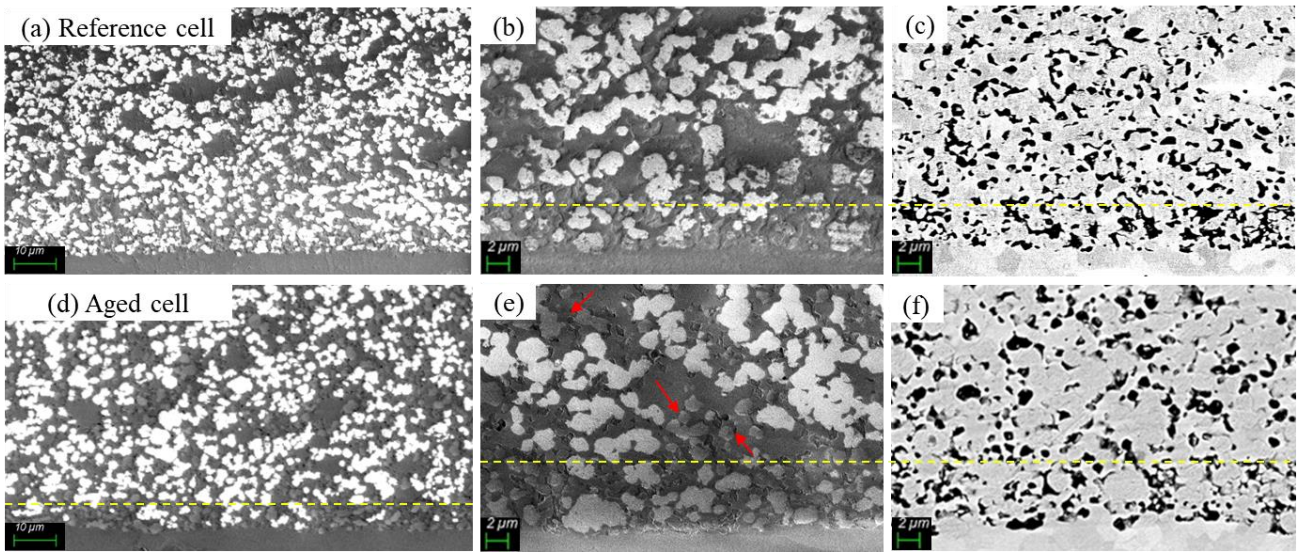

Fig. 7 Images of the Ni-YSZ fuel electrode for the reference cell (a-c) and the aged cell (d-f). (a-b) and (d-e) are low-voltage SEM images, while (c) and (f) are BSD images. In low-voltage SEM images: percolating Ni is white and non-percolating Ni is light gray. In BSD images, porosity is black.

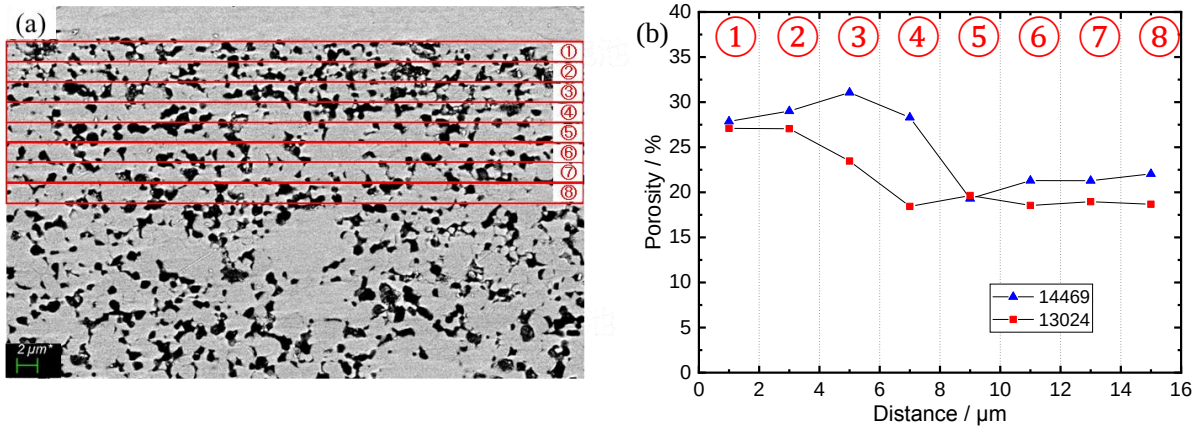

Fig. 8 BSD images used for the porosity quantification (a) and obtained results (b).

In the above post-mortem analysis, depletion of percolating Ni, Ni coarsening and change of pore morphology were mainly observed in the aged cell, which can cause damage to the cell performance. In the Ni-YSZ fuel electrode, the roles of Ni particles and YSZ skeleton are to conduct electrons and oxygen ions, respectively. The area where Ni, YSZ and pore come into contact is called three-phase boundaries (TPB). The electrochemical reactions of fuel electrodes occur at TPB in the region of a few microns close to the electrolyte. If Ni particles lose percolation or electrically connected, they cannot provide electrons and the electrochemical reactions will not take place there. This reduces the reaction sites, resulting in the increment of the resistance related to charge transfer reaction of fuel electrode. Meanwhile, this makes the reaction area away from the electrolyte and lengthens the oxygen ion transport path, which accordingly increases ohmic resistance. It is not difficult to understand that the Ni migration away from the electrolyte/fuel electrode interface will have the same effect. The Ni particles coarsening will decrease TPB length and primarily increase the resistance related to charge transfer reaction of fuel electrode. The pore microstructure mainly affects the gas diffusion process.

Combined with our previous study [21] and electrochemical analysis in this paper, the rapid Ni coarsening at the active layer/support layer interface caused by the Ni particle size difference was believed to be the dominant degradation mechanism of fast performance degradation in the initial stage. While in the stable stage, the slow coarsening and non-percolation of Ni particles led to a slow and linear decline in performance. Moreover, the change of pore morphology may be due to the combined effect of reduction in nickel oxide-nickel reaction and Ni sintering coarsening. Jiao et al. [56,57] have reported the competition between the mechanisms of reduction in nickel oxide-nickel reaction and Ni sintering coarsening in the reduction process. Therefore, it is reasonable to speculate that the further reduction of Ni particles may be the dominant reason for the decrease of the resistance related to gas diffusion process in the initial stage, and the increase of the resistance may be due to Ni sintering coarsening in the stable stage. More detailed researches are required to verify this conjecture.

To inhibit the microstructure changes in Ni-YSZ electrode and improve the stability, several methods have been proposed, such as optimizing the Ni-YSZ electrode microstructure [10], infiltrating GDC nanoparticles into the conventional Ni-YSZ electrode [54] and operating temperature selection at thermoneutral voltage [17]. However, the long-term degradation behavior of SOCs still need more in-depth and comprehensive research, i.e., balancing mechanisms for performance and stability, switching between fuel-cell and electrolysis modes, etc.

4. Conclusion

In this work, fuel-cell, electrolysis, and reversible operations of an industrial-size SOC (10 cm × 10 cm) were conducted to investigate the performance evolution mechanisms. The j-V curves and EIS measurements were periodically carried out. And the EIS data were analyzed to quantify the contribution of electrode processes employing the DRT method and ECM fitting.

The asymmetry behavior between the fuel-cell and electrolysis modes was found, that is, the resistances corresponding to the electrode processes held different change trends with increasing DC biases in the two modes. Moreover, the proportion of the resistance related to the gas diffusion and conversion processes of the fuel electrode was higher in the electrolysis mode, indicating that optimizing the fuel electrode microstructure to promote the gas diffusion process is an effective method to reduce asymmetry and increase the electrolysis performance. The evolution trend of resistances was basically the same under different DC biases. Compared with the fuel-cell mode, the resistances related to the charge transfer reaction, gas diffusion and conversion processes of fuel electrode increased faster in the electrolysis mode, suggesting more severe microstructure degradation. Future work should focus on improving performance and stability in the electrolysis mode.

Besides, through the evolution of j-V curves and resistances of electrode processes, the whole operation process was divided into the initial stage and the stable stage. The cell performance first showed slight change and rapidly declined subsequently in the initial stage, while decreasing slowly and linearly in the stable stage. In the post-mortem analysis, Ni non-percolating, Ni coarsening and change of pore morphology in the fuel electrode were mainly observed. Combined with the detailed EIS analysis and our previous studies, we believe that the rapid Ni coarsening at the active layer/support layer interface due to the Ni particle size difference was the dominant degradation mechanism of fast performance degradation in the initial stage. While in the stable stage, the slow and linear decline in performance resulted from the slow coarsening and non-percolation of Ni particles. Moreover, reduction in NiO-Ni reaction and Ni sintering coarsening together affected the pore morphology, and thus the gas diffusion process of the fuel electrode. The further reduction of NiO may

dominate and enhance the gas diffusion process in the initial stage, while Ni coarsening may dominate and weaken the gas diffusion process in the stable stage. More in-depth and comprehensive research is needed to inhibit the microstructure changes in Ni-YSZ electrode and investigate the long-term degradation behavior of SOCs.

CRediT authorship contribution statement

Tonghui Cui: Conceptualization, Methodology, Investigation, Writing – original draft. **Zewei Lyu:** Methodology, Investigation, Writing – review & editing. **Minfang Han:** Resources, Supervision, Writing – review & editing. **Kaihua Sun:** Resources, Validation. **Yang Liu:** Investigation, Validation. **Meng Ni:** Investigation, Writing – review & editing.

Declaration of competing interest

The authors declare that they have no known competing financial interests or personal relationships that could have appeared to influence the work reported in this paper

Acknowledgements

This work is supported by the National Natural Science Foundation of China (NSFC 5201101243) , and Tsinghua University State Key Lab Program (SKLD21M15). The authors would like to acknowledge colleagues in Tsinghua SOFC Lab and Huatsing Energy group for technical assistance and fruitful discussions.

References

1 Hauch, A. *et al.* Recent advances in solid oxide cell technology for electrolysis. *Science* **370**, doi:10.1126/science.aba6118 (2020).

2 Schwarze, K., Posdziech, O., Mermelstein, J. & Kroop, S. Operational Results of an 150/30 kW RSOC System in an Industrial Environment. *Fuel Cells*, doi:10.1002/fuce.201800194 (2019).

3 Mermelstein, J. & Posdziech, O. Development and Demonstration of a Novel Reversible SOFC System for Utility and Micro Grid Energy Storage. *Fuel Cells* **17**, 562-570, doi:10.1002/fuce.201600185 (2017).

4 Graves, C., Ebbesen, S. D., Jensen, S. H., Simonsen, S. B. & Mogensen, M. B. Eliminating degradation in solid oxide electrochemical cells by reversible operation. *Nat Mater* **14**, 239-244, doi:10.1038/nmat4165 (2015).

5 Frey, C. E., Fang, Q., Sebold, D., Blum, L. & Menzler, N. H. A Detailed Post Mortem Analysis of Solid Oxide Electrolyzer Cells after Long-Term Stack Operation. *Journal of the Electrochemical Society* **165**, F357-F364, doi:10.1149/2.0961805jes (2018).

6 Rinaldi, G. *et al.* Post-test Analysis on a Solid Oxide Cell Stack Operated for 10,700 Hours in Steam Electrolysis Mode. *Fuel Cells* **17**, 541-549, doi:10.1002/fuce.201600194 (2017).

7 Wilde, V. *et al.* Gd0.2Ce0.8O2 Diffusion Barrier Layer between (La0.58Sr0.4)(Co0.2Fe0.8)O3−δ Cathode and Y0.16Zr0.84O2 Electrolyte for Solid Oxide Fuel Cells: Effect of Barrier Layer Sintering Temperature on Microstructure. *ACS Applied Energy Materials* **1**, 6790-6800, doi:10.1021/acsaem.8b00847 (2018).

8 Menzler, N. H., Sebold, D., Sohn, Y. J. & Zischke, S. Post-test characterization of a solid oxide fuel cell after more than 10 years of stack testing. *Journal of Power Sources* **478**, doi:10.1016/j.jpowsour.2020.228770 (2020).

9 Trini, M. *et al.* Comparison of microstructural evolution of fuel electrodes in solid oxide fuel cells and electrolysis cells. *Journal of Power Sources* **450**, doi:10.1016/j.jpowsour.2019.227599 (2020).

10 Hauch, A., Brodersen, K., Chen, M. & Mogensen, M. B. Ni/YSZ electrodes structures optimized for increased electrolysis performance and durability. *Solid State Ionics* **293**, 27-36, doi:10.1016/j.ssi.2016.06.003 (2016).
11 Sun, X., Hendriksen, P. V., Mogensen, M. B. & Chen, M. Degradation in Solid Oxide Electrolysis Cells During Long Term Testing. *Fuel Cells* **19**, 740-747, doi:10.1002/fuce.201900081 (2019).
12 Tao, Y., Ebbesen, S. D. & Mogensen, M. B. Degradation of solid oxide cells during co-electrolysis of steam and carbon dioxide at high current densities. *Journal of Power Sources* **328**, 452-462, doi:10.1016/j.jpowsour.2016.08.055 (2016).
13 Rao, M., Jensen, S. H., Sun, X. & Hagen, A. Unwinding Entangled Degradation Mechanisms in Solid Oxide Electrolysis Cells Through Electrode Modifications and Impedance Analysis. *Fuel Cells*, doi:10.1002/fuce.201800166 (2019).
14 Tao, Y., Ebbesen, S. D. & Mogensen, M. B. Carbon Deposition in Solid Oxide Cells during Co-Electrolysis of H2O and CO2. *Journal of The Electrochemical Society* **161**, F337-F343, doi:10.1149/2.079403jes (2014).
15 Lyu, Z., Shi, W. & Han, M. Electrochemical characteristics and carbon tolerance of solid oxide fuel cells with direct internal dry reforming of methane. *Applied Energy* **228**, 556-567, doi:10.1016/j.apenergy.2018.06.114 (2018).
16 Chen, M. *et al.* Microstructural Degradation of Ni/YSZ Electrodes in Solid Oxide Electrolysis Cells under High Current. *Journal of The Electrochemical Society* **160**, F883-F891, doi:10.1149/2.098308jes (2013).
17 Yang, Y. *et al.* Study of solid oxide electrolysis cells operated in potentiostatic mode: Effect of operating temperature on durability. *Chem. Eng. J.* **417**, doi:10.1016/j.cej.2021.129260 (2021).
18 Hjalmarsson, P., Sun, X., Liu, Y.-L. & Chen, M. Influence of the oxygen electrode and inter-diffusion barrier on the degradation of solid oxide electrolysis cells. *Journal of Power Sources* **223**, 349-357, doi:10.1016/j.jpowsour.2012.08.063 (2013).
19 Hubert, M. *et al.* Impact of Nickel agglomeration on Solid Oxide Cell operated in fuel cell and electrolysis modes. *Journal of Power Sources* **397**, 240-251, doi:10.1016/j.jpowsour.2018.06.097 (2018).
20 Mogensen, M. B. *et al.* Ni migration in solid oxide cell electrodes: Review and revised hypothesis. *Fuel Cells*, doi:10.1002/fuce.202100072 (2021).
21 Lyu, Z. *et al.* Quantifying the performance evolution of solid oxide fuel cells during initial aging process. *Journal of Power Sources* **510**, doi:10.1016/j.jpowsour.2021.230432 (2021).
22 Brus, G. *et al.* Local evolution of anode microstructure morphology in a solid oxide fuel cell after long-term stack operation. *Journal of Power Sources* **288**, 199-205, doi:10.1016/j.jpowsour.2015.04.092 (2015).
23 Geng, J. *et al.* Comparative study on solid oxide fuel cell anode microstructure evolution after long-term operation. *Journal of Power Sources* **495**, doi:10.1016/j.jpowsour.2021.229792 (2021).
24 The, D. *et al.* Microstructural comparison of solid oxide electrolyser cells operated for 6100 h and 9000 h. *Journal of Power Sources* **275**, 901-911, doi:10.1016/j.jpowsour.2014.10.188 (2015).
25 Holzer, L. *et al.* Microstructure degradation of cermet anodes for solid oxide fuel cells: Quantification of nickel grain growth in dry and in humid atmospheres. *Journal of Power Sources* **196**, 1279-1294, doi:10.1016/j.jpowsour.2010.08.017 (2011).
26 Pihlatie, M. H., Kaiser, A., Mogensen, M. & Chen, M. Electrical conductivity of Ni–YSZ composites: Degradation due to Ni particle growth. *Solid State Ionics* **189**, 82-90, doi:10.1016/j.ssi.2011.02.001 (2011).
27 Nelson, G. J. *et al.* Three-dimensional microstructural changes in the Ni–YSZ solid oxide fuel cell anode during operation. *Acta Mater.* **60**, 3491-3500, doi:10.1016/j.actamat.2012.02.041 (2012).
28 Monaco, F. *et al.* Degradation of Ni-YSZ Electrodes in Solid Oxide Cells: Impact of Polarization and Initial Microstructure on the Ni Evolution. *Journal of The Electrochemical Society* **166**, F1229-F1242,

doi:10.1149/2.1261915jes (2019).

29 Hauch, A., Ebbesen, S. D., Jensen, S. H. & Mogensen, M. Solid Oxide Electrolysis Cells: Microstructure and Degradation of the Ni/Yttria-Stabilized Zirconia Electrode. *Journal of The Electrochemical Society* **155**, doi:10.1149/1.2967331 (2008).

30 Mogensen, M. B. *et al.* Relation Between Ni Particle Shape Change and Ni Migration in Ni-YSZ Electrodes - a Hypothesis. *Fuel Cells* **17**, 434-441, doi:10.1002/fuce.201600222 (2017).

31 Hauch, A., Jørgensen, P. S., Brodersen, K. & Mogensen, M. Ni/YSZ anode – Effect of pre-treatments on cell degradation and microstructures. *Journal of Power Sources* **196**, 8931-8941, doi:10.1016/j.jpowsour.2011.01.009 (2011).

32 Ebbesen, S. D. & Mogensen, M. Electrolysis of carbon dioxide in Solid Oxide Electrolysis Cells. *Journal of Power Sources* **193**, 349-358, doi:10.1016/j.jpowsour.2009.02.093 (2009).

33 Koch, S., Mogensen, M., Hendriksen, P. V., Dekker, N. & Rietveld, B. Electrode Activation and Passivation of Solid Oxide Fuel Cell Electrodes. *Fuel Cells* **6**, 117-122, doi:10.1002/fuce.200500111 (2006).

34 Lyu, Z., Li, H., Wang, Y. & Han, M. Performance degradation of solid oxide fuel cells analyzed by evolution of electrode processes under polarization. *Journal of Power Sources* **485**, doi:10.1016/j.jpowsour.2020.229237 (2021).

35 Sumi, H., Shimada, H., Yamaguchi, Y., Yamaguchi, T. & Fujishiro, Y. Degradation evaluation by distribution of relaxation times analysis for microtubular solid oxide fuel cells. *Electrochimica Acta* **339**, doi:10.1016/j.electacta.2020.135913 (2020).

36 Zhang, Y., Han, M. & Sun, Z. High performance and stability of nanocomposite oxygen electrode for solid oxide cells. *International Journal of Hydrogen Energy* **45**, 5554-5564, doi:10.1016/j.ijhydene.2019.05.027 (2020).

37 Lu, L. *et al.* Long-term stability of carbon dioxide electrolysis in a large-scale flat-tube solid oxide electrolysis cell based on double-sided air electrodes. *Applied Energy* **259**, doi:10.1016/j.apenergy.2019.114130 (2020).

38 Fang, Q., Frey, C. E., Menzler, N. H. & Blum, L. Electrochemical Performance and Preliminary Post-Mortem Analysis of a Solid Oxide Cell Stack with 20,000 h of Operation. *Journal of The Electrochemical Society* **165**, F38-F45, doi:10.1149/2.0541802jes (2018).

39 Fang, Q. *et al.* Degradation Analysis of an SOFC Short Stack Subject to 10,000 h of Operation. *Journal of The Electrochemical Society* **167**, doi:10.1149/1945-7111/abc843 (2020).

40 Tong, X., Hendriksen, P. V., Hauch, A., Sun, X. & Chen, M. An Up-scalable, Infiltration-Based Approach for Improving the Durability of Ni/YSZ Electrodes for Solid Oxide Cells. *Journal of The Electrochemical Society* **167**, doi:10.1149/1945-7111/ab6f5c (2020).

41 Thyden, K. Microstructural characterization of SOFC Ni–YSZ anode composites by low-voltage scanning electron microscopy. *Solid State Ionics* **178**, 1984-1989, doi:10.1016/j.ssi.2007.12.075 (2008).

42 Rao, M., Sun, X. & Hagen, A. A Comparative Study of Durability of Solid Oxide Electrolysis Cells Tested for Co-Electrolysis under Galvanostatic and Potentiostatic Conditions. *Journal of The Electrochemical Society* **165**, F748-F755, doi:10.1149/2.0151810jes (2018).

43 Talic, B., Venkatachalam, V., Hendriksen, P. V. & Kiebach, R. Comparison of MnCo2O4 coated Crofer 22 H, 441, 430 as interconnects for intermediate-temperature solid oxide fuel cell stacks. *Journal of Alloys and Compounds* **821**, doi:10.1016/j.jallcom.2019.153229 (2020).

44 Shi, W., Jia, C., Zhang, Y., Lü, Z. & Han, M. Differentiation and Decomposition of Solid Oxide Fuel Cell Electrochemical Impedance Spectra. *Acta Physico-Chimica Sinica* **35**, 509-516, doi:10.3866/pku.Whxb201806071 (2019).

45 Cui, T. *et al.* Identification of Electrode Process in Large-size Solid Oxide Fuel Cell. *Acta Physico Chimica Sinica* **0**, 2011009-2011000, doi:10.3866/pku.Whxb202011009 (2020).
46 Leonide, A., Sonn, V., Weber, A. & Ivers-Tiffée, E. Evaluation and Modeling of the Cell Resistance in Anode-Supported Solid Oxide Fuel Cells. *Journal of The Electrochemical Society* **155**, doi:10.1149/1.2801372 (2008).
47 Sonn, V., Leonide, A. & Ivers-Tiffée, E. Combined Deconvolution and CNLS Fitting Approach Applied on the Impedance Response of Technical Ni/8YSZ Cermet Electrodes. *Journal of The Electrochemical Society* **155**, doi:10.1149/1.2908860 (2008).
48 Primdahl, S. & Mogensen, M. Gas Conversion Impedance: A Test Geometry Effect in Characterization of Solid Oxide Fuel Cell Anodes. *Journal of The Electrochemical Society* **145**, 2431-2438, doi:10.1149/1.1838654 (1998).
49 Caliandro, P., Nakajo, A., Diethelm, S. & Van herle, J. Model-assisted identification of solid oxide cell elementary processes by electrochemical impedance spectroscopy measurements. *Journal of Power Sources* **436**, doi:10.1016/j.jpowsour.2019.226838 (2019).
50 Lyu, Z., Han, M., Sun, Z. & Sun, K. Evolution of Electrochemical Characteristics of Solid Oxide Fuel Cells During Initial-Stage Operation. *Acta Chim. Sinica* **79**, doi:10.6023/a21020065 (2021).
51 Wang, Y., Lyu, Z., Han, M., Sun, Z. & Sun, K. Initial-Stage Performance Evolution of Solid Oxide Fuel Cells Based on Polarization Analysis. *ECS Transactions* **103**, 1261-1269, doi:10.1149/10301.1261ecst (2021).
52 Kishimoto, M., Tanimura, Y., Seo, H., Iwai, H. & Yoshida, H. Asymmetric behavior of solid oxide cells between fuel cell and electrolyzer operations. *International Journal of Hydrogen Energy*, doi:10.1016/j.ijhydene.2021.07.093 (2021).
53 Ebbesen, S. D., Sun, X. & Mogensen, M. B. Understanding the processes governing performance and durability of solid oxide electrolysis cells. *Faraday Discuss.* **182**, 393-422, doi:10.1039/c5fd00032g (2015).
54 Ovtar, S. *et al.* Boosting the performance and durability of Ni/YSZ cathode for hydrogen production at high current densities via decoration with nano-sized electrocatalysts. *Nanoscale* **11**, 4394-4406, doi:10.1039/c8nr07678b (2019).
55 Jiao, Z., Busso, E. P. & Shikazono, N. Influence of Polarization on the Morphological Changes of Nickel in Fuel Electrodes of Solid Oxide Cells. *Journal of The Electrochemical Society* **167**, doi:10.1149/1945-7111/ab6f5b (2020).
56 Jiao, Z. & Shikazono, N. Quantitative Study on the Correlation between Solid Oxide Fuel Cell Ni-YSZ Composite Anode Performance and Reduction Temperature Based on Three-Dimensional Reconstruction. *Journal of The Electrochemical Society* **162**, F571-F578, doi:10.1149/2.0721506jes (2015).
57 Jiao, Z., Ueno, A., Suzuki, Y. & Shikazono, N. Study on the influences of reduction temperature on nickel-yttria-stabilized zirconia solid oxide fuel cell anode using nickel oxide-film electrode. *Journal of Power Sources* **328**, 377-384, doi:10.1016/j.jpowsour.2016.08.043 (2016).